Atmospheric Research 288 (2023) 106727

Contents lists available at ScienceDirect

Atmospheric Research

journal homepage: www.elsevier.com/locate/atmosres

Large-scale climatic drivers for warm-season compound drought and heatwave frequency over North China

Jing Wang [a], Mingcai Li [a,*], Yanju Liu [b,*], Jinxin Zhang [c], Xiao Zheng [c]

[a] Tianjin Key Laboratory for Oceanic Meteorology, Tianjin Institute of Meteorological Science, Tianjin 300074, China
[b] National Climate Center, China Meteorological Administration, Beijing 100081, China
[c] Qingyuan Forest CERN, CAS Key Laboratory of Forest Ecology and Management, Institute of Applied Ecology, Chinese Academy of Sciences, Shenyang 110016, China

ARTICLE INFO

Keywords:
Compound drought and heatwave frequency
North China
Warm season
Climatic drivers
Maritime continent

ABSTRACT

Based on multiple observational and reanalysis datasets, this study investigated the large-scale climatic drivers responsible for the warm season (April to September) compound drought and heatwave (CDHW) frequency over the North China (NC) domain, both locally and remotely. The warm-season NC CDHW frequency exhibited salient year-to-year variation. We identified that the extensive equivalent barotropic high-pressure anomaly centered around Lake Baikal could be the predominant local-scale driving factor. In addition, the low-pressure circulation anomaly to the southeast played a secondary dynamic amplification role. Such a dipole pattern can jointly cause more frequent occurrences of NC CDHWs by triggering anomalies in localized meteorological variables (e.g., surface warming and drying) and land surface variable (reduced soil moisture) that are favorable for CDHW formation during the warm season. Regarding remote driving factors, central eastern Maritime Continent (MC) convection centered over New Guinea could be an influential and direct atmospheric forcing factor. Meanwhile, the sea surface temperature (SST) anomaly pattern over the tropical eastern Pacific (TEP) was identified as a crucial oceanic forcing indirectly modulating the NC CDHW frequency through the critical medium of MC convection. Through a Hadley-like meridional overturning circulation pattern, the suppressed MC convection can remotely induce a dipolar pattern similar to that related to a higher NC CDHW frequency, exerting a so-called direct modulation effect. Furthermore, positive TEP SST anomalies act as anomalous Rossby wave sources via anomalous upper-tropospheric divergence, characterized by westward-propagating descending Rossby waves with notable wave energy advecting westward toward the central–eastern MC. In such a scenario, a reversed Walker-like circulation pattern can form to sustain the suppressed MC convection, playing an intermediate role in the maintenance of the high-pressure anomaly centered around Lake Baikal. Our findings may provide new insights into the synergistic roles of distant climatic driving factors in the modulation and maintenance of interannual variations of warm-season NC CDHW.

1. Introduction

A plethora of studies have reported that, under the context of global climatic warming, more frequent occurrences of droughts and heatwaves can be detected, posing considerably deleterious/negative impacts on socioeconomic development, water storage, ecosystem, agrarian production, human health, and wildfire risk in multiple domains across the globe (e.g., Easterling et al., 2000; Wilhite, 2000; CDC, 2004; Ciais et al., 2005; Seneviratne et al., 2014; Perkins, 2015; Watts et al., 2015; Su et al., 2018; Zscheischler et al., 2018; Vautard et al., 2019; Chen et al., 2022a, 2022b; Hao et al., 2022; He et al., 2022; Hettiarachchi et al., 2022; Kong et al., 2020; Libonati et al., 2022). Accordingly, droughts and heatwaves are two major influential climatic hazards around the world (e.g., Wilhite, 2000; Easterling et al., 2000; Ciais et al., 2005; Dai, 2013; Hao et al., 2018a), becoming popular topics across sections of the climate community worldwide (e.g., Dai, 2013; Kiem et al., 2016; Xu et al., 2019; Yeo et al., 2019; Cook et al., 2020; Ma et al., 2020; Eischeid et al., 2022; Ha et al., 2022; Ham et al., 2022; Jiang et al., 2022; Meque et al., 2022). When specifically focusing on China, many publications documented that eastern China is highly vulnerable to frequent droughts and heatwaves due to the dense populations and flourishing economy (e.g., Zhang and Zhou, 2015; Gao et al., 2018; Yu

---

* Corresponding authors.
E-mail addresses: li_mingcai@163.com (M. Li), liuyanj@cma.gov.cn (Y. Liu).

https://doi.org/10.1016/j.atmosres.2023.106727
Received 7 December 2022; Received in revised form 19 March 2023; Accepted 19 March 2023

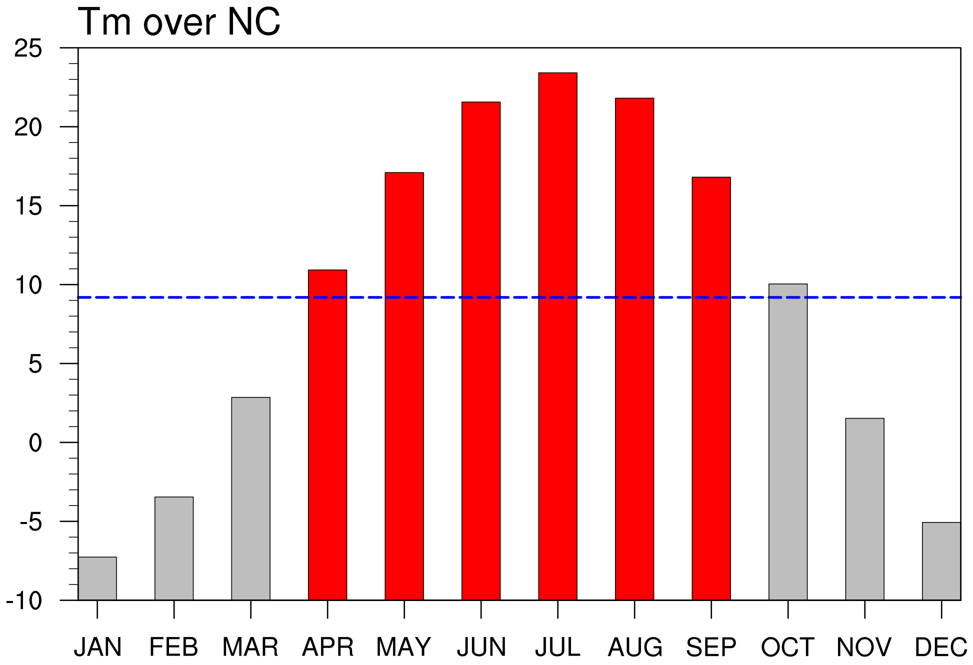

Fig. 1. The Climatological-mean monthly evolution of 2-m T_m (°C; bars) over the research domain of North China (NC; 35°–42°N, 110°–120°E), in which the red bars indicate the warm season (April–September; AMJJAS). The base period is 1981–2010. The horizontal blue dashed line denotes the average annual 2-m T_m. The CN05.1 dataset is used. (For interpretation of the references to colour in this figure legend, the reader is referred to the web version of this article.)

and Zhai, 2020a, 2020b; Li et al., 2021a; Jiang et al., 2022; Wang et al., 2022b; Zhang et al., 2022). For instance, Jiang et al. (2022) reported an extreme drought event that hit southeastern China and its surroundings from May to October 2019, causing crop damage of >3.3 million hectares and resulting in tremendous economic losses. Moreover, a record-breaking (since 1961) peak-summer heatwave hit Zhejiang Province, China, in 2022, inducing severe power shortages, drought conditions, and multiple deaths resulting from sunstroke (https://m.thepaper.cn/baijiahao_20181208).

It is worthy of stressing the compound drought and heatwave (CDHW) phenomenon (Zscheischler et al., 2018; Hao et al., 2018a, 2022), which has received notable increasing attention across the globe recently [e.g., the United States (Mazdiyasni and AghaKouchak, 2015), the Southeast Brazil (Geirinhas et al., 2021), and India (Sharma and Mujumdar, 2017)]. This could be because CDHWs can exert more profoundly amplified detrimental impacts than the linear superposition of their univariate counterparts, even though the univariate components may not be extreme themselves (Hao et al., 2022). The corresponding intensified magnitude of hazardous impacts can be attributed to active land-air coupling/feedback under concurrent hot and dry environments (Alexander, 2011; Perkins, 2015). More specifically, high overlying air temperatures can drastically increase drought intensity by enhancing potential evapotranspiration, thereby triggering pronounced soil moisture deficiency (Dai, 2013). Dry surface conditions associated with depleted soil moisture can release more sensible heat into the ambient air by reducing evaporative cooling, which in turn enhances the overlying heat intensity (Alexander, 2011; Seneviratne et al., 2010; Greve et al., 2014).

Furthermore, extensive efforts have been devoted to the climatic drivers of CDHWs variability over multiple areas across the globe (e.g., Luo et al., 2020; Ali et al., 2021; Ionita et al., 2021; Hao et al., 2022), highlighting the critical modulatory roles of large-scale high-pressure systems/anticyclonic circulations in situ, which may be embedded in atmospheric teleconnected patterns. These systems/circulations are linked to locally favorable meteorological conditions, such as suppressed cloud cover with elevated downward solar radiation flux and descending motion anomalies with adiabatic heating anomalies, which excite surface warming (Gao et al., 2018; Li et al., 2021a; Jiang et al., 2022; Hao et al., 2022). For example, Gao et al. (2018) revealed that a localized descending high-pressure anomaly linked to the western Pacific subtropical high could trigger notable surface warming in the Yangtze–Huaihe River Basin during the peak summer by strengthening the positive downward solar radiation flux caused by suppressed cloud cover. Additionally, the formation and maintenance of CDHWs at global and/or regional scales (e.g., mainland China) could be significantly modulated by remote large-scale modes of sea surface temperature (SST) variability, such as the El Niño–Southern Oscillation (ENSO) (Hao et al., 2018b; Wu et al., 2021), thus serving as effective external forcings contributing to the climate variability of CDHWs. Note that many existing studies concentrated on exploring spatiotemporal characteristics and climatic driving factors for summertime CDHW events across the globe, arguably owing to the fact that the most intensive compounding stresses of dry and hot extremes occur in summer (Hao et al., 2018a; Kong et al., 2020; Yu and Zhai, 2020b).

Notably, statistical findings revealed that the North China (NC) domain [35°–42°N, 110°–120°E] ranks among the top hotspot regions for the climate extremes of CDHWs during the warm season, which is consistent with the center of high CDHW frequency over northern China (north of 35°N) (Kong et al., 2020; Yu and Zhai, 2020a, 2020b). However, considering the complicated climate of China, in this study, we defined the warm season as the six months from April to September (AMJJAS) for the NC domain based on the monthly evolution of the 2-m mean air temperature (T_m). During the warm season of AMJJAS, T_m was clearly higher than the corresponding average annual value, together with a prominent T_m increase (decrease) from March to April (September to October) (Fig. 1). In northern China, our defined warm season coincides exactly with the period favorable for surface ozone formation (Lu et al., 2018, 2020), and largely matches the crop-growing season (Xiong et al., 2014; Yu et al., 2014) and the terrestrial vegetation-growing season (Song et al., 2010). Frequent NC CDHWs during the warm season exacerbate surface ozone pollution (Wang et al., 2022a), exerting highly detrimental impacts on human health (Zhang et al., 2019). Additionally, frequent CDHWs during warm seasons can significantly reduce vegetation productivity (Zhang et al., 2016). Therefore, identifying the influential drivers and understanding the associated physical causes responsible for the higher warm-season CDHW frequency in NC could be of particular importance for dealing with regional ozone-induced human health issues and potential low vegetation/crop productivity issues during the growing season.

In northern China, various studies have explored large-scale climatic drivers of hot summer events. For instance, Ding et al. (2020) and Li et al. (2020) suggested that extreme heat events are related to large-scale midlatitude continental high-pressure anomalies. This anticyclonic anomaly could be regulated by zonal planetary-scale wave train circulation anomalies across the Atlantic and Europe, which could have been excited by upstream northern North Atlantic SST anomalies (SSTAs) during the previous winter and spring. The factors driving CDHEs may vary in different regions, seasons, and time scales (Zhang et al., 2021; Hao et al., 2022). Droughts and heatwaves show pronounced interannual variations (e.g., Gao et al., 2018; Yeo et al., 2019; Li et al., 2021a; Ham et al., 2022). Despite the numerous studies conducted, the climatic drivers and associated physical causes responsible for NC warm-season CDHWs on an interannual timescale remain elusive. This knowledge gap motivated us to identify the physico-meteorological drivers for the interannual variability of the NC warm-season CDHWs, both locally and remotely, with the aim of shedding light on the corresponding driving mechanisms. Such knowledge could facilitate a deeper understanding of the interannual variability in CDHW frequency in NC. More importantly, in the context of the recent global warming in terms of heat extremes and droughts (Iyakaremye et al., 2021; Ullah et al., 2022a, 2022b), the present research may provide a basis for policy-makers to formulate adaptation and mitigation strategies for warm-season NC CDHEs. The remainder of this paper is organized as follows. Section 2 describes the data and methods used in the study. In Section 3, we explore the regional and faraway large-scale driving factors tied to the interannual variability of warm-season CDHW frequency in NC and investigate the underlying physical mechanisms sustaining the higher CDHW frequency. Finally, the major conclusions and associated discussions are presented in Section 4.

2. Data and methods

2.1. Datasets

The datasets used in this study consist of the following:

1. High-resolution gridded observational datasets from the National Climate Center of China (CN05.1; Wu and Gao, 2013) were employed to calculate compound drought and heatwave frequency, including monthly precipitation and daily 2-m maximum air temperature (T_{max}) and T_m, with a horizontal resolution of 0.25° × 0.25°.
2. Monthly atmospheric reanalysis data were provided by the National Centers for Environmental Prediction (NCEP)–Department of Energy (DOE) AMIP-II reanalysis (NCEP-2; Kanamitsu et al., 2002). The spatial resolution for pressure-level data was 2.5° × 2.5°, whilst, for 2-m meteorological parameters, total cloud cover, surface flux, and surface volumetric soil moisture at 0–10 cm (SM10cm), the spatial resolution was T62 (192 × 94 points in the horizontal direction).
3. Monthly Merged Analysis of Precipitation (CMAP) data with a horizontal resolution of 2.5° × 2.5°were obtained from the Climate Prediction Center (Xie and Arkin, 1997).
4. Monthly outgoing longwave radiation (OLR) data were obtained from the National Oceanic and Atmospheric Administration (NOAA) (Liebmann and Smith, 1996), with a horizontal resolution of 2.5° × 2.5°.
5. Monthly SST data were obtained from NOAA Extended Reconstructed SST version 5 (ERSST5; Huang et al., 2017), with a horizontal resolution of 2° × 2°.
6. Monthly vertical integrals of eastward and northward total energy flux (TEF; $\overrightarrow{F}$ for short) data (abbreviated as F_x and F_y, respectively) from the fifth major global reanalysis produced by the ECMWF (ERA5; Hersbach et al., 2020), with a horizontal resolution of 0.25° × 0.25°.

All datasets used in this study focused on the boreal warm season (April–September; AMJJAS; Fig. 1), covering the period 1979–2018.

2.2. Definitions

Following the approach of Kong et al. (2020), we employ the standardized precipitation index (SPI), which is a commonly used indicator for monitoring drought states at multiple timescales (Mckee et al., 1993; Hayes et al., 2011; Hao et al., 2017), to examine drought conditions. For the detailed algorithm for calculating SPI, readers can refer to He et al. (2022). A drought month was identified when the corresponding 1-month SPI value was smaller than −1 (Kong et al., 2020). Further, we define the local heat extremes by adopting the relative daily T_{max} definition threshold (viz. the 90th–percentile-based threshold), rather than the absolute daily T_{max} definition threshold [e.g., 35 °C (Gao et al., 2018) and 33 °C (Yeo et al., 2019)], because the relative threshold metric could be more useful to identify local heat extremes (Wang et al., 2017). Hence, we determined a heatwave day (HD) as a day with T_{max} exceeding the 90th percentile of the corresponding daily T_{max} over the base period 1981–2010, which is in accordance with many previous studies (e.g., Kong et al., 2020; Li et al., 2021a; Serrano-Notivoli et al., 2022). Based on the above definitions, the monthly compound drought and HDs in the present study were defined as the total number of HDs in the corresponding drought month, which served as a measure of the monthly CDHW frequency. As such, the warm-season CDHW frequency over NC can be measured as the grid mean (based on CN05.1 datasets) of the AMJJAS-accumulated drought-month HDs within the entire NC domain (abbreviated as $\mathrm{DHD_{NC}}$). It is worth noting that the above metric of domain-averaged $\mathrm{DHD_{NC}}$ can significantly reduce the noise at each grid and facilitate the understanding of the physical processes responsible for large-scale atmospheric and oceanic anomalies (Gao et al., 2018; Li et al., 2021a).

2.3. Methods

Following Sardeshmukh and Hoskins (1988), the Rossby wave source (RWS) can be calculated as

$$RWS = -\nabla\cdot\left[V_{\chi}(\zeta + f)\right], \tag{1}$$

where V_{χ}represents the divergent wind, ζrepresents the relative vorticity, and f represents the planetary vorticity.

The vertically integrated horizontal water vapor transport (⟨WVT⟩) and associated divergence (⟨WVT_div⟩) were calculated using the following equations (Sun et al., 2019; Li et al., 2021b):

$$\langle \mathrm{WVT} \rangle = -\frac{1}{g}\int_{Ps}^{300} q\overrightarrow{V}dp, \tag{2}$$

$$\langle \mathrm{WVT\_}div \rangle = -\frac{1}{g}\int_{Ps}^{300} \nabla_{p}\cdot\left(q\overrightarrow{V}\right)dp, \tag{3}$$

where $\nabla_p\ \cdot$ ()denotes the horizontal divergence in the pressure coordinates; g is the gravitational acceleration; P_s is the surface pressure; q is the specific humidity; and $\overline{V} = (u, v)$ is the horizontal wind vector (u and v represent the zonal and meridional winds, respectively).

The horizontal divergence of the TEF ($\nabla\cdot\overrightarrow{F}$) and the associated divergent (i.e., irrotational) horizontal components of$\overrightarrow{F}$were used to examine the energy transport from the tropical eastern Pacific (TEP). Here, the vector$\overrightarrow{F} = (F_x, F_y)$. Based on the divergence$\nabla\cdot\overrightarrow{F}$, we computed

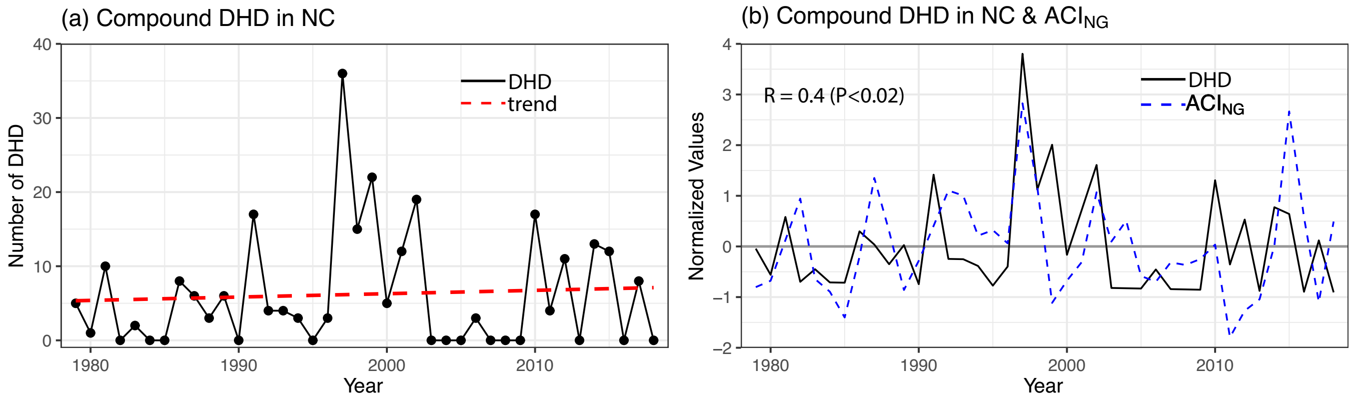

Fig. 2. (a) Time series of the warm-season (AMJJAS) compound DHD$_{NC}$ (days) during 1979–2018. (b) Normalized and detrended time series of AMJJAS-accumulated compound DHD$_{NC}$ (black line), along with the concurrent New Guinean atmospheric convective index (ACI$_{NG}$; blue line), for the period 1979–2018. In panel (b), the numeral labeled at the upper-left corner represents the temporal correlation coefficient (TCC) between DHD$_{NC}$ and ACI$_{NG}$. (For interpretation of the references to colour in this figure legend, the reader is referred to the web version of this article).

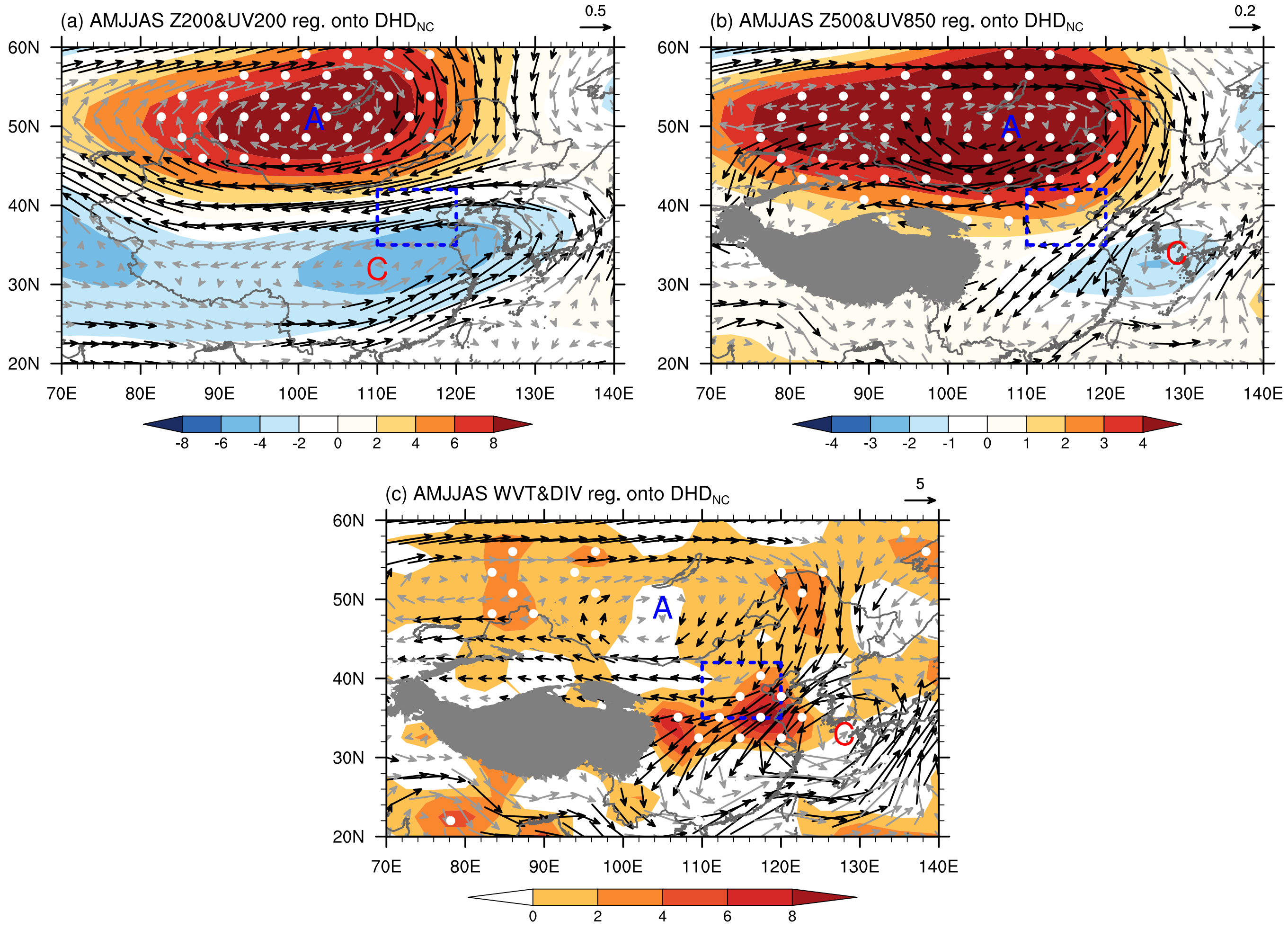

Fig. 3. Regressed anomalies of AMJJAS-mean (a) 200-hPa geopotential height (Z200; gpm; shading) and wind field (UV200; m s^{-1}; vectors), (b) 500-hPa geopotential height (Z500; gpm; shading) and 850-hPa wind field (UV850; m s^{-1}; vectors), and (c) <WVT> (kg m^{-1} s^{-1}; vectors) and < WVT_div > (10^{-6} kg m^{-2} s^{-1}; shading), with respect to the concurrent normalized warm-season compound DHD$_{NC}$ during 1979–2018. All variables are detrended. Black arrows indicate anomalies of vectors significant at the 90% confidence level. Areas with significant values of Z200, Z500, and < WVT_div > exceeding 90% confidence level are dotted. Letter A (C) represents the center of anticyclonic (cyclonic) anomaly (the same hereinafter) in terms of the horizontal quivers. The grey-shaded areas denote the Tibetan Plateau (the same hereinafter). The blue dashed frame outlines the research domain of NC (35°–42°N, 110°–120°E; the same hereinafter). (For interpretation of the references to colour in this figure legend, the reader is referred to the web version of this article).

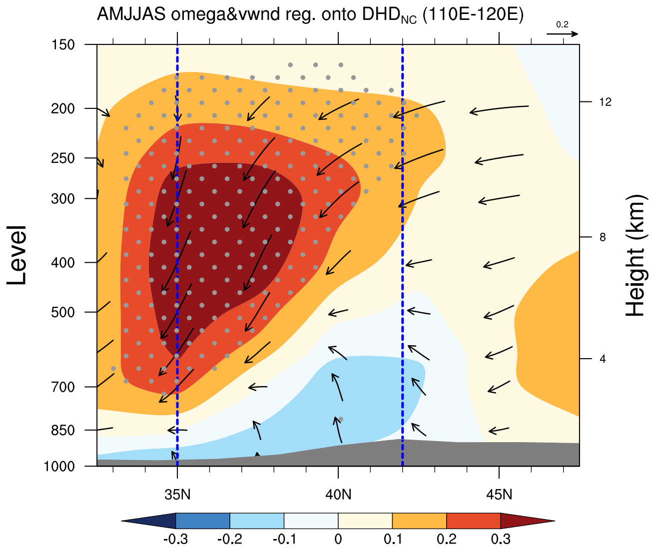

Fig. 4. Height–latitude cross-section of AMJJAS-mean omega (10^{-2} Pa s^{-1}; shading) and vertical wind (m s^{-1}; vectors) anomalies regressed onto the concurrent normalized warm-season compound DHD$_{NC}$ averaged along 110°-120°E during 1979–2018. All variables are detrended. Omega anomalies that are significant at the 90% confidence level are stippled. The blue-dashed vertical lines represent the latitudinal range of the research domain of NC (35°–42°N). The grey shading indicates the topography. (For interpretation of the references to colour in this figure legend, the reader is referred to the web version of this article).

the divergent horizontal component of $\vec{F}$ ($\vec{F}_{\text{div}}$ for short) via the spherical harmonics technique. For convenience in highlighting the large-scale features of $\nabla\cdot\vec{F}$ and the associated divergent component of $\vec{F}$, the TEF data were bilinearly interpolated to a horizontal resolution of 2.5° × 2.5° beforehand, identical to that of NCEP-2.

Following the recommendation of Vicente-Serrano et al. (2010), the monthly potential evapotranspiration (PET) is estimated via the Thornthwaite method (Thornthwaite, 1948).

To exclude the potential impacts of long-term trends in the variables, all data and time series were linearly detrended before further calculations focused on interannual variations (Huangfu et al., 2022; Zhang et al., 2022). Furthermore, climate time series can contain a seasonal component. This is a cycle that repeats over time, which may contribute to a high correlation between any of the two climatic variables. The reason is that the same location on the Earth obtains regularly-varying solar radiation, which largely controls the behavior of many climatic variables at a seasonal time scale. Hence, to remove the possible influence of seasonality, we removed the seasonal cycle of each variable by subtracting the climatology of the corresponding calendar month (Zhou et al., 2011; Yang et al., 2022). A two-tailed Student's *t*-test was used to evaluate the statistical significance.

3. Results

3.1. Regional-scale circulation patterns tied to interannual warm-season NC CDHW frequency anomalies

Before mining the dominant circulation anomaly pattern responsible for the interannual variability of the warm-season CDHW frequency over the NC domain, it was necessary to identify the main characteristics of the temporal variation in the warm-season NC CDHW frequency. As shown in Fig. 2, the warm-season CDHW frequency over NC exhibited salient year-to-year variations. There was a much higher warm-season CDHW frequency in certain years, such as 1997, 1999, and 2002, with the highest frequency in 1997 (Fig. 2a), while an extremely low frequency was observed in certain years, such as 2003 following 2002, 2016, and 2018, which have zero CDHW days (Fig. 2a). Furthermore, the CDHW frequency exhibits a slightly increasing trend (Fig. 2a). We further present the detrended and normalized time series of the AMJJAS-accumulated compound DHD$_{NC}$ for the period 1979–2018, which shows evident interannual fluctuations with positive/negative values (Fig. 2b; black line). Note that we merely explored climatic anomalies tied to warm-season higher NC CDHW frequency (i.e., positive compound DHD$_{NC}$-regressed anomalies), which is the main focus of the present research.

Next, we revealed the dominant regional-scale circulation patterns associated with a higher warm-season NC CDHW frequency. Fig. 3 depicts linear regressed patterns of AMJJAS-mean circulations at different tropospheric levels as well as <WVT> and associated divergence onto the simultaneous CDHW frequency. As shown in Figs. 3a–b, the more frequent occurrences of CDHWs correspond well to a clear large-scale high-pressure (anticyclonic circulation) anomaly centered around Lake Baikal, which is dominated by an equivalent barotropic structure. This anomalous anticyclone covers extensive northern Asian domains, with the main body spanning from northern Kazakhstan to northeastern China (Figs. 3a–b). Numerous previous studies have demonstrated that the high-pressure system serves as a critical circulation driver, triggering positive CDHW frequency anomalies over many regions across the globe by modulating variations in areal precipitation, moisture, and temperature (e.g., Perkins, 2015; Li et al., 2021a; Jiang et al., 2022; Wang et al., 2022b). In this study, however, we indicate that the relatively small cyclonic anomaly southeast of the giant anticyclonic anomaly (Figs. 3a–b) also plays a dynamic amplification role. The corresponding driving mechanism is described as follows: First, the high-pressure anomaly can transport dry cold advection from mid-to-high latitudes to NC and its adjoining areas via significant northeasterly anomalies on the eastern flank (Figs. 3a, b, and 4). Second, with the aid of a low-pressure system that strengthened the pressure gradient surrounding the NC domain, significant northeasterly anomalies predominated the entire NC at the mid-to-upper tropospheric levels (Figs. 3a, b, and 4). Note that the low-pressure system is contracted and shifts more eastward in the lower troposphere (Fig. 3b), with its center appearing south of the Korean Peninsula, thus inducing significant low-low northeasterly anomalies that dominate the southeastern portion of NC (Figs. 3b and 4). Such equivalent barotropic dipolar pattern connects a large clockwise < WVT > gyre pattern centered to the south of Lake Baikel and a small anticlockwise < WVT > gyre pattern centered to the south of the Korean Peninsula (Fig. 3c), triggering local positive <WVT_div > anomalies with much greater magnitudes over the southeastern part, which can greatly inhibit the inflow of moist air into the NC domain.

Under the aforementioned favorable dynamical and thermodynamical circumstances, the vigorous integrated dry air divergence and the concomitant downward motion anomalies can induce striking suppressed cloud cover/rainfall with clear sky conditions (Figs. 5a, d), thereby sparking pronounced adiabatic atmospheric heating and enhanced shortwave radiations (Fig. 5b) to induce localized surface warming (Fig. 5c), elevated PET (Fig. 5e), and reduced anomalies of surface specific humidity (Fig. 5f) and soil moisture (Fig. 5g), with much greater magnitudes in the southern/southeastern part of the NC domain. Anomalies of negative precipitation and positive PET can lead to an enhanced water imbalance, inducing significant drought conditions (Wang et al., 2022b). Moreover, through soil moisture-atmosphere coupling, surface air warming and drying, together with suppressed soil moisture, are conducive to the maintenance of heatwaves under drought conditions (Alexander, 2011; Perkins, 2015; Alizadeh et al., 2020), suggesting a vigorous interplay between droughts and heatwaves (Seneviratne et al., 2010; Miralles et al., 2019). Consequently, positive warm-season NC CDHW frequency anomalies are induced.

However, the large centers of positive shortwave radiation (Fig. 5b) and surface warming (Fig. 5c) were not consistent. A plausible reason could be that, in addition to radiation, the variation in surface air

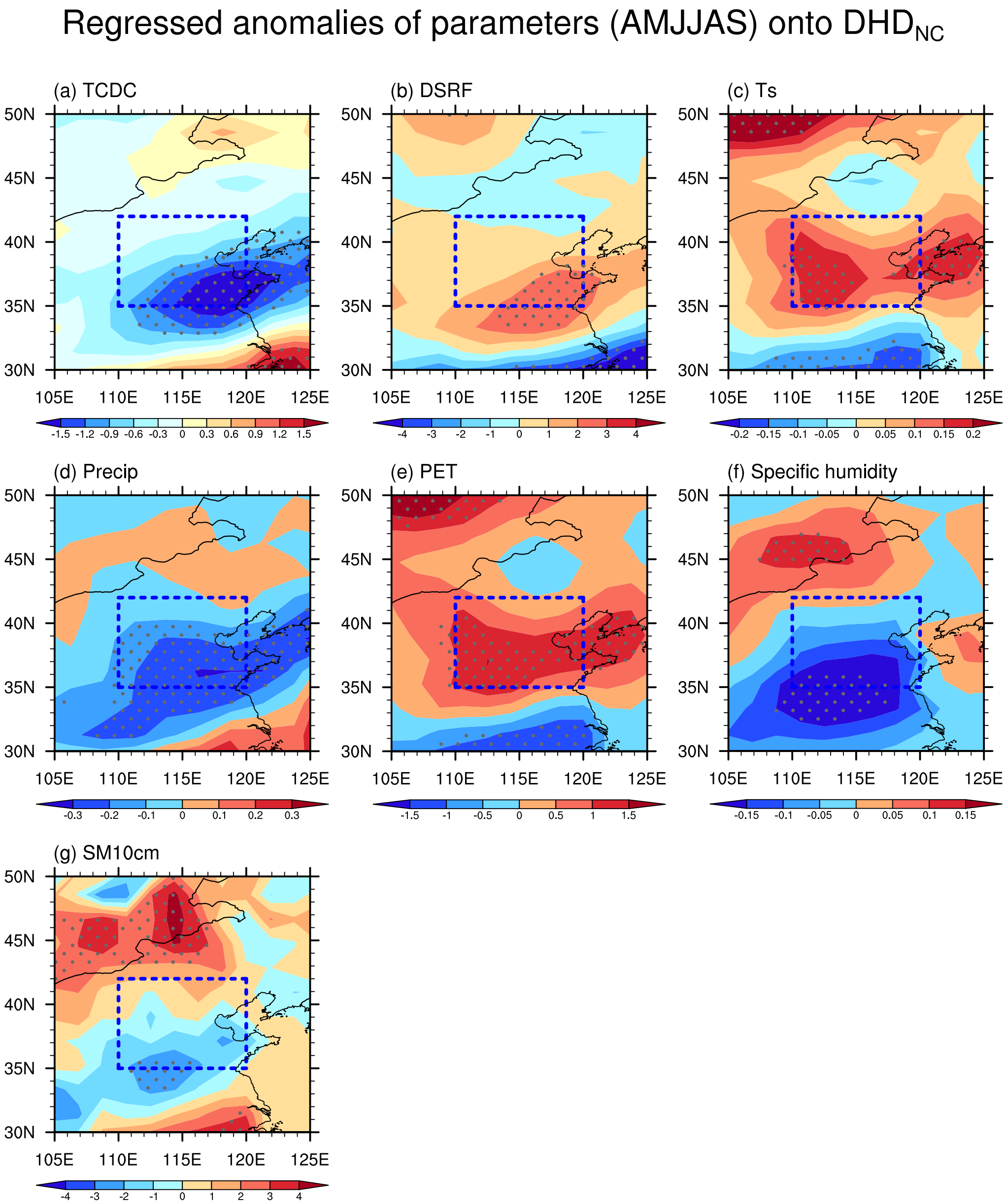

Fig. 5. Regressed anomalies of AMJJAS-mean meteorological and land surface parameters onto the concurrent normalized warm-season compound DHD_{NC} during 1979–2018, including (a) total cloud cover (%; shading), (b) downward solar radiation flux (W m^{-2}; shading), (c) 2-m air temperature (°C; shading), (d) precipitation (mm day^{-1}; shading), (e) PET (mm $month^{-1}$; shading), (f) 2-m specific humidity (g kg^{-1}; shading), and (g) SM10cm (m^3 m^{-3}; shading). All variables are detrended. Downward solar radiation flux anomalies are defined as positive downward. Regression coefficients that are significant at the 90% confidence level are stippled.

temperature can also be modulated by other factors, such as horizontal and vertical temperature advection processes (Feng et al., 2014). Furthermore, although northeasterly anomalies can bring anomalous cold air into NC (Figs. 3–4), the resultant descent anomalies can induce and maintain notable positive adiabatic atmospheric heating and radiation anomalies (Fig. 5), thus outweighing the opposite effects of cold air intrusion. Similar physical processes were found in the causal analysis of severe droughts in Southwest China during the local dry season (Feng et al., 2014).

Overall, we suggest that the large-scale equivalent barotropic high-pressure anomaly centered around Lake Baikal is the predominant circulation pattern that induces a higher CDHW frequency. Furthermore, the low-pressure system to the southeast played a secondary dynamic amplification role. Such a dipole pattern could synergistically trigger meteorological and land surface variables that favor more frequent occurrences of warm-season NC CDHWs. In the subsequent sections, we explore the remote driving factors associated with a higher interannual warm-season NC CDHW frequency.

3.2. *Remote atmospheric and oceanic drivers for interannual warm-season NC CDHW frequency anomalies*

Many previous studies have identified that the interannual variations in droughts and heatwaves in East Asian regions can be driven by remote atmospheric and oceanic variabilities, highlighting the zonal Rossby wave train stemming from the North Atlantic and the well-organized meridional overturning pattern originating around the Maritime Continent (MC) and Philippine Sea, which may be induced and sustained by SST anomaly patterns over the North Atlantic Ocean and the tropical Indo-Pacific Ocean, respectively (e.g., Jiang et al., 2017; Yeo et al., 2019; Jiang et al., 2022). Hence, the question arises as to the major remote climatic drivers of the higher interannual warm-season NC CDHW frequency. To further address this question, we first presented planetary-scale atmospheric (i.e., OLR/precipitation and lower-level winds) and oceanic (i.e., SST) variabilities associated with simultaneous positive warm-season CDHW frequency anomalies over NC (Fig. 6) to identify significant drivers. As shown in Figs. 6a–b, pronounced extensive atmospheric responses (i.e., positive OLR/negative precipitation anomalies) tended to occur over the areas around the

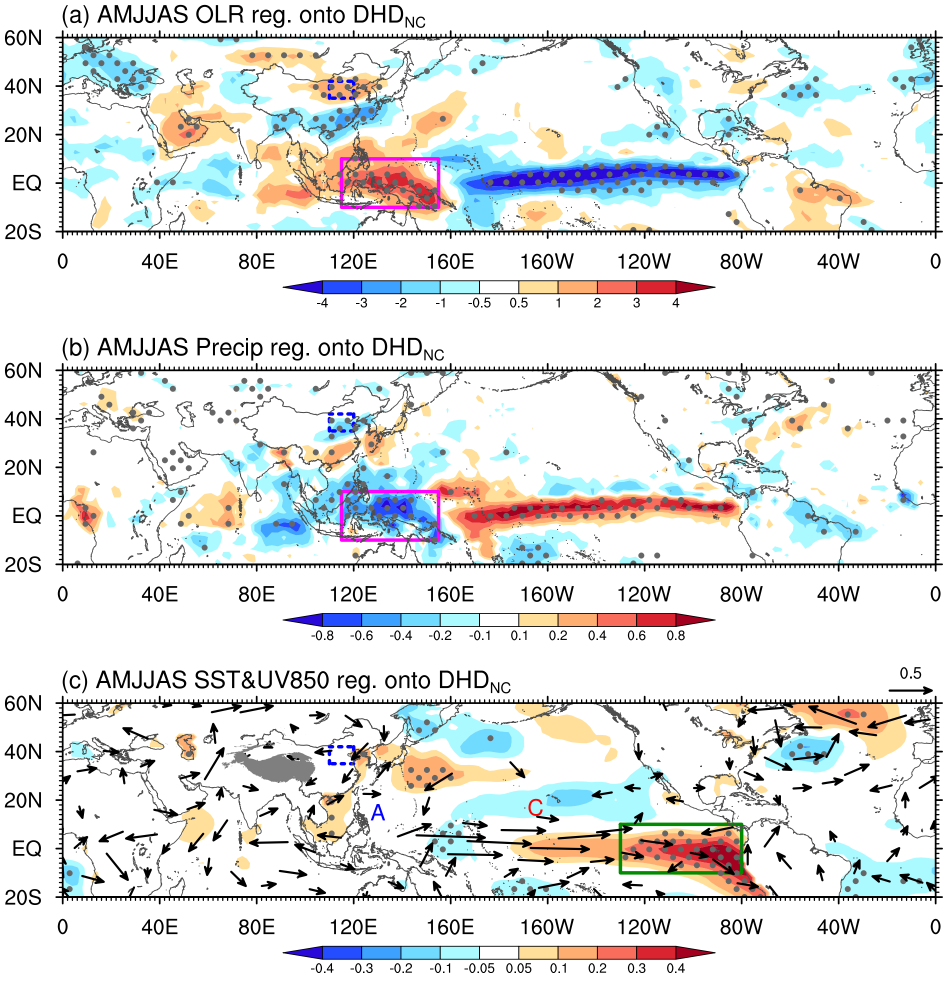

Fig. 6. Identification of major remote climatic drivers of the interannual warm-season NC CDHW frequency. Regressed anomalies of AMJJAS-mean (a) OLR (W m^{-2}; shading), (b) precipitation (mm day^{-1}; shading), and (c) SST (°C; shading) and UV850 (m s^{-1}; vectors) onto the concurrent normalized warm-season compound DHD$_{NC}$ during 1979–2018. All variables are detrended. Regression coefficients that are significant at the 90% confidence level are stippled. Only wind vectors that are significant t at the 90% confidence level are shown. In panels (a) and (b), the magenta box (10°S-10°N, 115°-155°E) indicates the key atmospheric convective region for defining ACI$_{NG}$ (the same hereinafter). In panel (c), the green rectangle (10°S-10°N, 130°-80°W) denotes the key tropical eastern Pacific area with significant regression coefficients (the same hereinafter). (For interpretation of the references to colour in this figure legend, the reader is referred to the web version of this article).

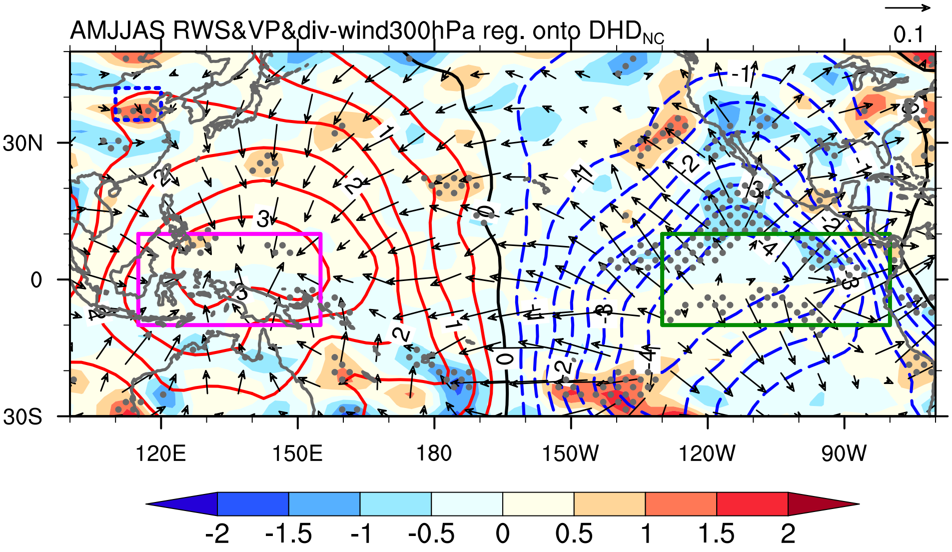

Fig. 7. Description of mechanisms and processes tied to the interannual warm-season NC CDHW frequency from the perspective of RWS theory. Regressed anomalies of AMJJAS-mean 300-hPa RWS (10^{-11} s^{-2}; shading), velocity potential (10^{5} m^{2} s^{-1}; contours; interval: 0.5), and divergent horizontal wind (m s^{-1}; vectors) onto the concurrent normalized warm-season compound DHD$_{NC}$ during 1979–2018. All variables are detrended. Areas with significant values of RWS exceeding 90% confidence level are dotted.

central-eastern MC, with the center appearing over New Guinea (NG), suggesting suppressed local convective activities. Additionally, a significant zonal atmospheric response belt was observed (Figs. 6a–b) in response to the key significant SST warming region over the TEP (Fig. 6c; green frame), which is consistent with the results of previous studies (Wang et al., 2000; Hu et al., 2021). However, only small patches of atmospheric and oceanic variability were detected over the North Atlantic (Fig. 6). In addition, according to the DHD$_{NC}$-associated teleconnection patterns within a larger domain (**Fig. S1**), we observed that the wave trains initiated from the North Atlantic in the middle and upper troposphere were interrupted over midlatitude western Europe with fairly weak height anomalies. The above results suggest that the

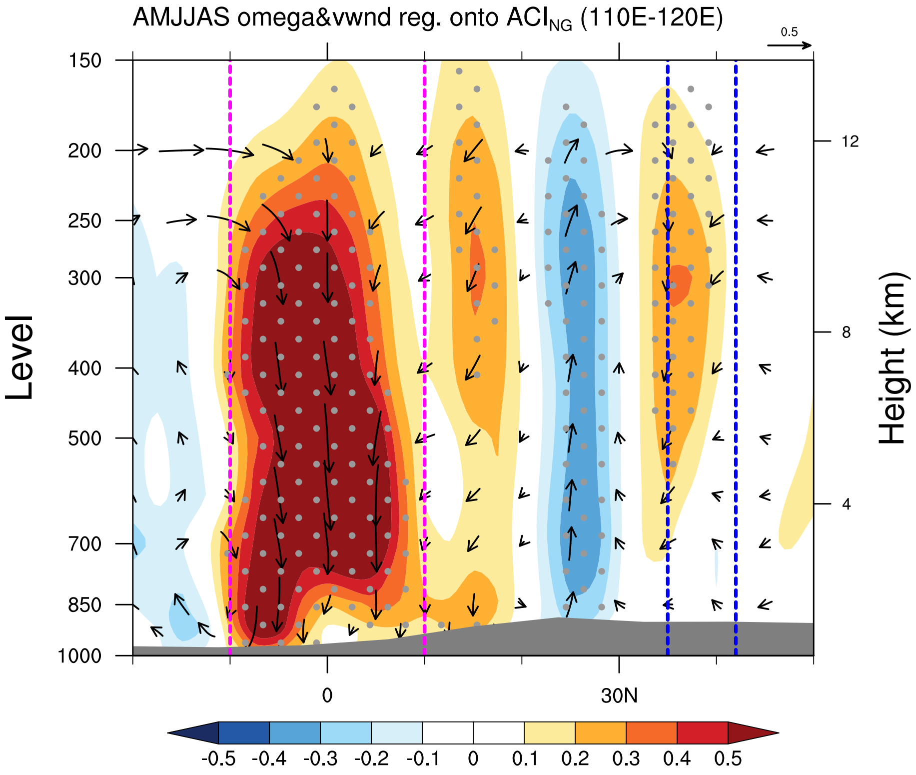

Fig. 8. Height–latitude cross-section of AMJJAS-mean omega (10^{-2} Pa s^{-1}; shading) and vertical wind (m s^{-1}; vectors) anomalies regressed onto the concurrent normalized ACI$_{NG}$ averaged along 110°-120°E during 1979–2018. All variables are detrended. Omega anomalies that are significant at the 90% confidence level are stippled. The magenta-dashed vertical lines indicate the latitudinal range of the key atmospheric convective region for defining ACI$_{NG}$ (10°S–10°N). The blue-dashed vertical lines represent the latitudinal range of the research domain of NC (35°–42°N). The grey shading indicates the topography. (For interpretation of the references to colour in this figure legend, the reader is referred to the web version of this article).

suppressed atmospheric convection activities centered on NG and TEP SST warming are the dominant remote large-scale driving factors conducive to more frequent occurrences of NC CDHWs, rather than the upstream zonal wave train induced by the North Atlantic SST anomaly pattern.

Furthermore, we describe mechanisms and processes tied to the interannual warm-season NC CDHW frequency from the perspective of RWS theory. Fig. 7 shows the anomalous patterns of the RWS, velocity potential, and divergent horizontal wind at 300 hPa regressed onto the warm-season compound DHD$_{NC}$. It can be clearly seen that the velocity potential anomalies exhibit a zonal negative-positive dipole pattern from east to west in the upper troposphere, with negative (positive) loadings surrounding the TEP (MC). Under these circumstances, extensive upper tropospheric divergence and negative RWS anomalies can be discerned over the TEP, and anomalous convergence and positive RWS can be observed over the MC, suggesting vigorous ascending (descending) motions and enhanced (dampened) convection activity over the TEP (MC) (Fig. 7). Correspondingly, divergent easterly anomalies flowed from the TEP to the central–eastern MC, whereas divergent westerly anomalies flowed from the eastern Indian Ocean to the central–eastern MC. The above analysis suggests the following two points. First, MC-suppressed convection activities centered over the NG may be a critical remote atmospheric driver, which may directly link the more frequent occurrences of NC CDHWs through the meridional wave-like pattern. A recent study identified that southeast China underwent an extremely hot drought event in August 2019 that was directly modulated by suppressed convective activities over the MC. Second, SST warming over the TEP may transmit its simultaneous influence through the intermediate atmospheric medium of the central eastern MC-suppressed convection, thus sustaining the interannual connection between the suppressed convection and higher NC CDHW frequency during the warm season. Similar physical pathways have been reported by Zhang and Duan (2021), who identified that the tropical Pacific–Indian Ocean SST mode can regulate the dipole mode of the October precipitation anomaly over the Tibetan Plateau via the key medium of suppressed concurrent northern MC convection. In the next section, we examine and demonstrate the above potential mechanisms and processes tied to our identified atmospheric and oceanic variabilities, aiming to understand their active roles in driving higher warm-season NC CDHW frequency.

3.3. Potential driving mechanisms

3.3.1. Direct modulation role of suppressed convection over the central-eastern MC

To quantitatively reveal the direct modulation effect of the central-eastern MC convection, following the method of Jiang et al. (2022), we first defined an atmospheric convection index (ACI) as the domain-averaged precipitation anomalies over the key region with the center located around NG (10S°–10°N, 115°–155°E; magenta frame in Fig. 6b). This index is multiplied by −1 to express the influence of the suppressed convection around NG, which is abbreviated as ACI$_{NG}$. Therefore, a positive ACI$_{NG}$ corresponds to a suppressed central-eastern MC convection. As shown in Fig. 2b, a salient in-phase relationship can be observed between the ACI$_{NG}$ and warm-season CDHW frequency over NC on the interannual time scale, with a temporal correlation coefficient (TCC) of 0.40 (p-value <0.02). Further analyses indicate that, from the perspective of the ACI$_{NG}$-regressed the vertical-meridional cross-section of the wind and omega anomalies (Fig. 8), we can conclude that the suppressed convection can remotely link higher NC CDHW frequencies through a well-organized Hadley-like meridional overturning circulation pattern, which can induce significant air subsidence anomalies over the NC domain with greater magnitudes in the central southern portion, as well as marked ascending motion anomalies to the south. Correspondingly, the dipolar circulation patterns and the <WVT> pattern can be formed (Fig. 9), which are generally similar to those shown in Fig. 3 although the magnitudes are weaker. As such, the ACI$_{NG}$-induced meteorological and land surface parameters were generally favorable for the formation of higher warm-season CDHW frequencies over NC, especially in the southern region (Fig. 10).

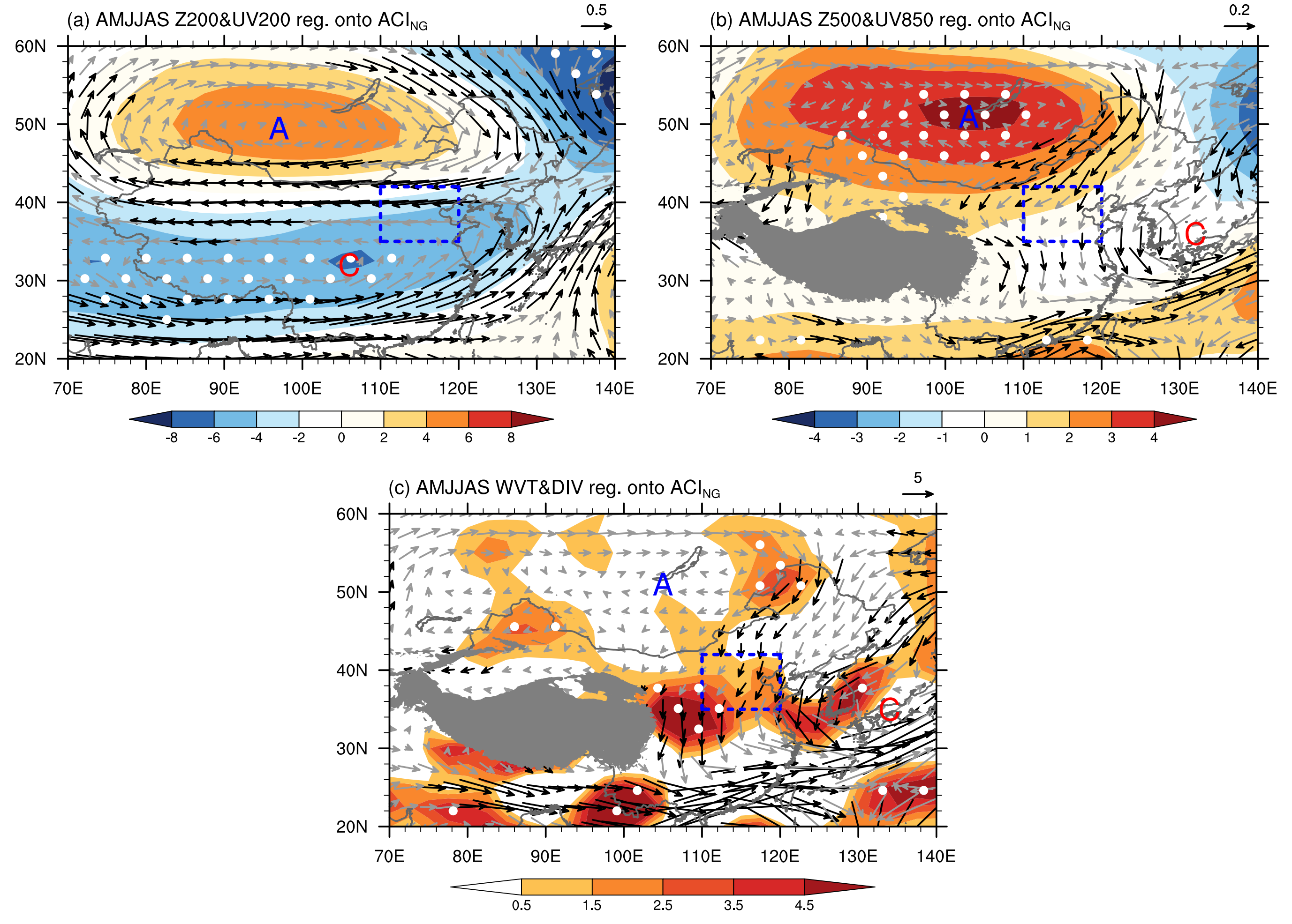

Fig. 9. As in Fig. 3, but with respect to ACI$_{NG}$.

3.3.2. *Maintenance effect of SST warming over the TEP*

Next, we explored the physical pathway by which SST warming over the TEP sustained suppressed convection over the central-eastern MC, which may therefore serve as an intermediate driving factor for the higher CDHW frequency over NC. Fig. 6c shows significant low-level westerly anomalies over the equatorial central-eastern Pacific, which could be an atmospheric response to the ENSO-like SST warming pattern (Wang et al., 2000; Hu et al., 2021). Under these circumstances, warm TEP SSTAs could stimulate a Gill-type response with a low-level cyclonic circulation anomaly northwest of the key TEP region (Fig. 6c) (Gill, 1980; Wang et al., 2009). Furthermore, we identified significant rainfall anomalies associated with warm TEP SSTAs. These atmospheric anomalies were observed more conspicuously in the corresponding SST$_{TEP}$-regressed anomalies, which had greater magnitudes (Fig. 11). Here, the SSTAs averaged over the critical warm region over the TEP (10S°–10°N, 130°–80°W; green frames in Figs. 6c and 11) in AMJJAS are defined as the SST$_{TEP}$. Notably, significant SST cooling also occurred over the western flank of the cyclonic anomaly (Fig. 11). This is excited by anomalous northeasterly winds that strengthen the climatological trade winds. Consequently, westward-propagating descending Rossby waves can be induced to enhance the anticyclonic anomaly over the western North Pacific (Wang et al., 2000, 2013) to trigger and sustain the suppressed convection over the central-eastern MC (Figs. 6c and 11). Furthermore, the regressions of the RWS, velocity potential and divergent horizontal wind anomalies at 300 hPa on the SST$_{TEP}$ are shown in Fig. 12a, whose spatial features are quite consistent with those shown in Fig. 7. We also exhibited SST$_{TEP}$-regressed anomalies of the TEF divergence and associated divergent components (Fig. 12b). The simultaneous TEF was transported from the TEP to the areas surrounding the central–eastern MC, indicating that the energy transportation was from the TEP. Under such circumstances, prominent reversed single-cell Walker-like circulation anomalies can be generated (Fig. 13a), with significant consistent ascending motion anomalies over the TEP and neighboring areas to the west, and the resultant remarkable air subsidence over the central-eastern MC. It can be clearly observed that the Walker-like circulation pattern related to the warm-season compound DHD$_{NC}$ is analogous to that related to warm TEP SSTAs, despite its relatively weak magnitude (Figs. 13a, b), thus showing that TEP SST warming is conducive to the occurrence of NC CDHWs.

In summary, in light of the above analyses, we can corroborate the assumption that SST warming over the TEP could be an effective oceanic driver sustaining suppressed convection over the central eastern MC, serving as an effective anomalous RWS through anomalous upper-tropospheric divergence according to the RWS theory (Sardeshmukh and Hoskins, 1988). Consequently, it exerted favorable intermediate maintenance effects on the critical large-scale high-pressure anomaly centered around Lake Baikal (Fig. 3) through suppressed MC convection, leading to more frequent occurrences of warm-season NC CDHWs.

4. Conclusions and discussion

Motivated by the scarcity of knowledge concerning the physical causes of the interannual warm-season (April to September) NC CDHW frequency anomalies, based on gridded observational data and

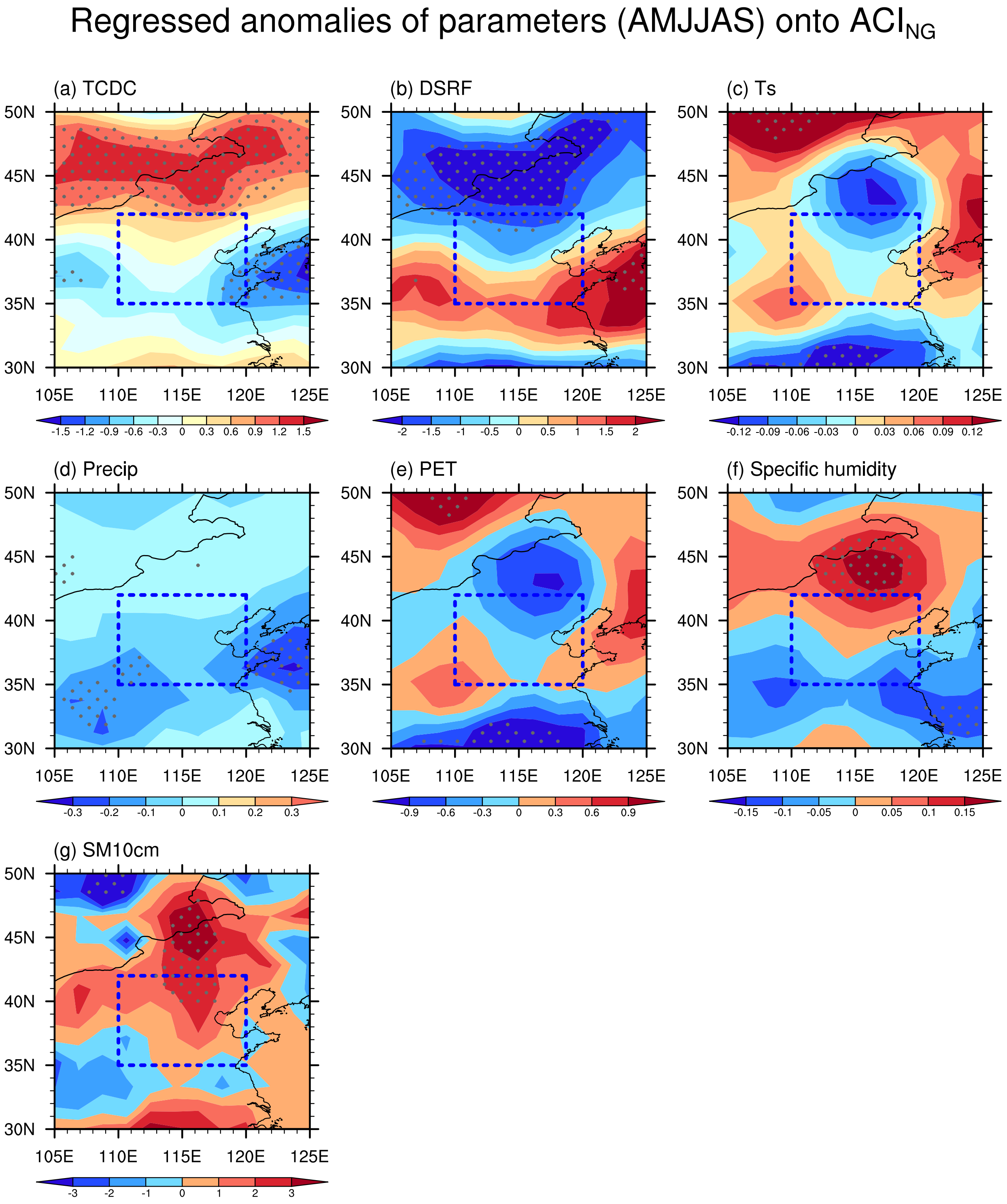

Fig. 10. As in Fig. 5, but onto ACI$_{NG}$.

reanalysis data from 1979 to 2018, this study aims to explore large-scale climatic drivers, both locally and remotely, and their possible driving mechanisms. The major conclusions are summarized as follows:

1. The warm-season CDHW frequency over the NC domain exhibited salient year-to-year changes with a slight upward trend. The corresponding predominant regional-scale circulation pattern is a continental high-pressure anomaly centered around Lake Baikal, with an equivalent barotropic structure extending from northern Kazakhstan to Northeast China. In addition, the low-pressure circulation anomaly to the southeast played a secondary dynamic amplification role. This dipolar pattern can collectively and effectively transport dry cold advection from mid-to-high latitudes to NC to excite vigorous dry air divergence and downward motion anomalies, with greater magnitudes over the southeastern part. This dipolar circulation regime can, by and large, excite local anomalies of meteorological variables (e.g., surface warming and drying) and land surface variable (suppressed soil moisture) favorable for the generation of compound heatwaves and droughts, thus causing more frequent occurrences of warm-season NC CDHWs.

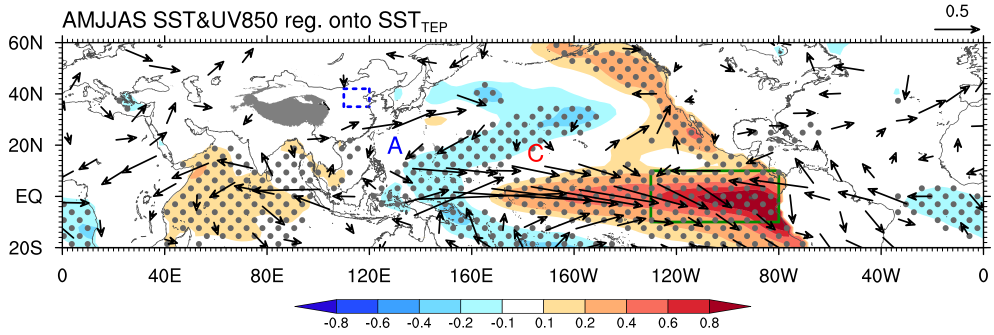

Fig. 11. As in Fig. 6c, but with respect to SST$_{TEP}$.

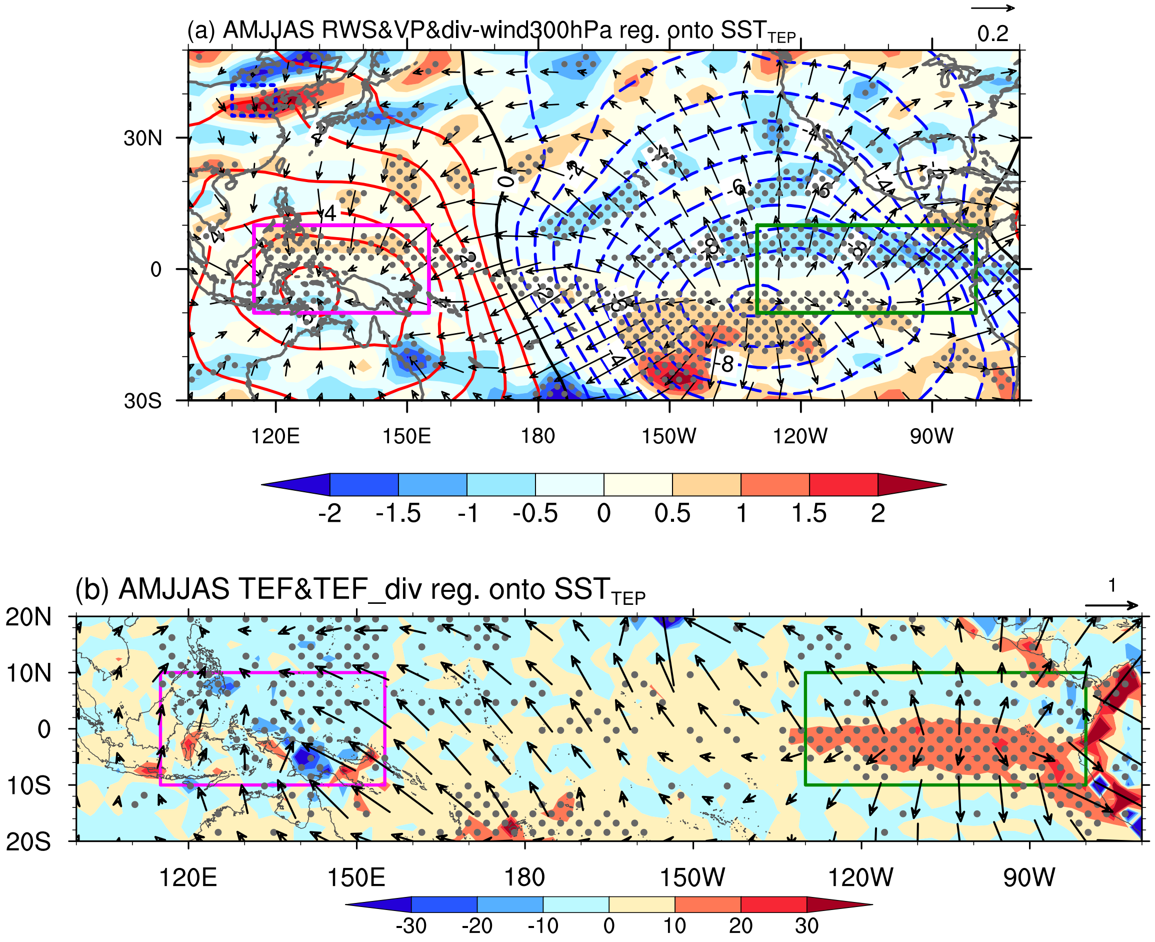

Fig. 12. Regressed anomalies of AMJJAS-mean (a) 300-hPa RWS (10^{-11} s^{-2}; shading), velocity potential (10^5 m^2 s^{-1}; contours; interval: 1), and divergent horizontal wind (m s^{-1}; vectors) and (b)$\nabla\cdot\vec{F}$ (W m^{-2}; shading) and$\vec{F}_{\mathrm{div}}$(10^7 W m^{-1}; vectors) onto the concurrent normalized SST$_{TEP}$ during 1979–2018. All variables are detrended. Areas with significant values of RWS and$\nabla\cdot\vec{F}$ exceeding 90% confidence level are dotted.

2. The suppressed central eastern MC convection with a notable center over the NG could be deemed a salient remote atmospheric forcing factor that can directly and significantly induce more frequent occurrences of warm-season NC CDHWs. Furthermore, the TEP SST warming pattern was identified as an influential distant oceanic forcing factor that indirectly caused a higher NC CDHW frequency through the critical atmospheric medium of suppressed MC convection.
3. Through a Hadley-like meridional overturning circulation pattern, the suppressed central–eastern MC convection can directly promote local circulation anomalies associated with the NC CDHW. In other words, suppressed MC convection can remotely induce a regional dipolar pattern resembling that tied to a higher warm-season NC CDHW frequency, exerting a direct modulation effect. Under these circumstances, meteorological and land surface parameter anomalies associated with suppressed MC convection are generally favorable for the formation of higher warm-season CDHW frequencies over the NC.
4. TEP SST warming can stimulate a Gill-type response with a low-level cyclonic circulation anomaly northwest of the key TEP region. As such, westward-propagating descending Rossby waves can be induced to enhance the anticyclonic anomalies over the western

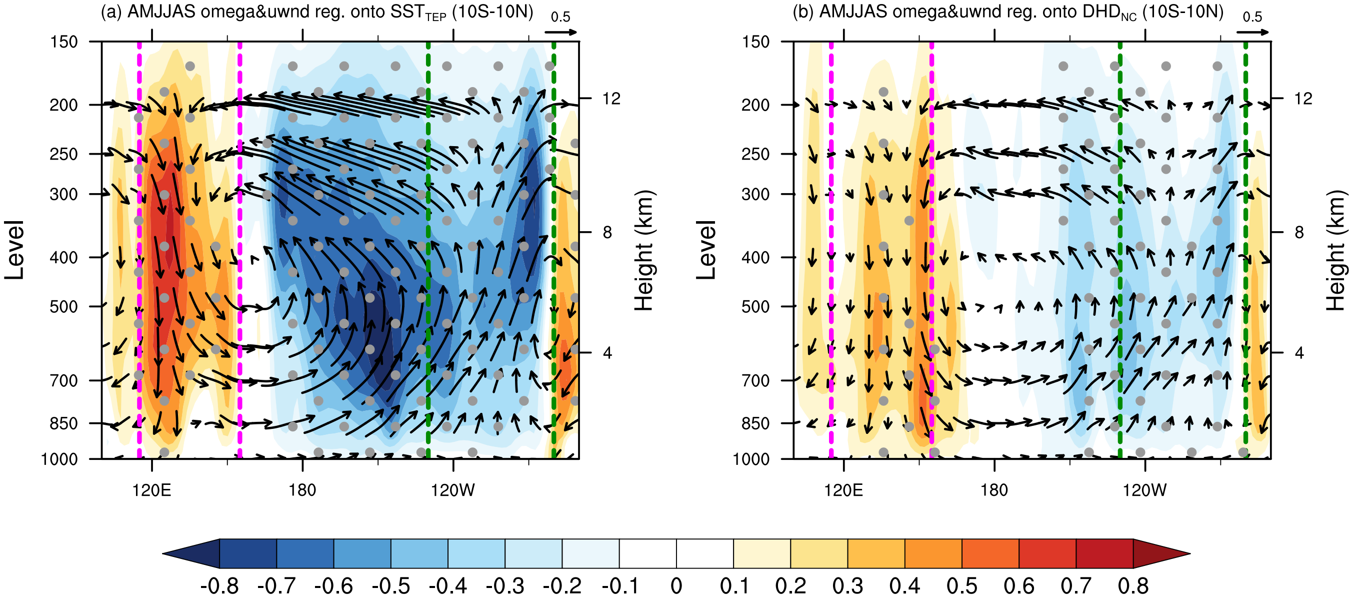

Fig. 13. Height–longitude cross-section of AMJJAS-mean omega (10^{-2} Pa s^{-1}; shading) and vertical wind (m s^{-1}; vectors) anomalies regressed onto the concurrent normalized (a) SST$_{TEP}$ and (b) warm-season compound DHD$_{NC}$ averaged along 10°S-10°N during 1979–2018. All variables are detrended. Omega anomalies that are significant at the 90% confidence level are stippled. The green-dashed vertical lines represent the longitudinal range of TEP (130°-80°W). The magenta-dashed vertical lines indicate the longitudinal range of the key atmospheric convective region for defining ACI$_{NG}$ (115°-155°E). (For interpretation of the references to colour in this figure legend, the reader is referred to the web version of this article).

North Pacific. Furthermore, in light of the RWS theory and simultaneous TEF transportation, TEP SST warming acts as an anomalous RWS via anomalous upper-tropospheric divergence, with notable wave energy propagating westward toward the central-eastern MC. In such a scenario, a reversed Walker-like circulation pattern similar to that associated with a higher warm-season NC CDHW frequency can be formed to sustain the suppressed MC convection, thereby playing an intermediate role in the maintenance of the critical large-scale high-pressure anomaly centered around Lake Baikal.

The following two points warrant further discussion. First, the limitations of the two remote drivers are acknowledged. That is, in contrast with the compound DHD$_{NC}$-regressed anticyclonic circulation patterns and $<$ WVT$>$ pattern, the ACI$_{NG}$-regressed ones are less extensive with weaker magnitudes (Fig. 3 vs. Fig. 9). In response, the ACI$_{NG}$-related anomalies of meteorological and land surface parameters were generally weakened, and stronger magnitudes of anomalies were confined to the southern portion of NC (Fig. 5 vs. Fig. 10). Therefore, although MC convection could be a major remote atmospheric driving factor modulating the interannual warm-season NC CDHW frequency, it only accounts for part of the interannual variance from the perspective of regional-scale circulation patterns. Further, lead-lag correlation results suggest that the interannual warm-season NC CDHW frequency exhibits quite insignificant connection with the preceding TEP SST anomaly pattern from the boreal winter (December to February) and early spring (March), with the TCCs of −0.09, −0.10, −0.06, and 0.11, respectively. Consequently, TEP SST warming with a significant simultaneous correlation may not act as a potential predictability source that physically contributes to higher NC CDHW frequency.

Second, we should point out that recent studies indicated that other driving factors, such as global warming (e.g., Dai, 2013; Coffel et al., 2018), the Arctic sea ice (e.g., Li et al., 2018), and the snow cover pattern (e.g., Yao et al., 2022), can drive the variations of droughts and heatwaves. Hence, identifying the climatic factors, especially the precursory factors driving the warm-season NC CDHW frequency, and exploring the associated modulation pathways warrant further investigation. In terms of current studies (e.g., Iyakaremye et al., 2021; Ullah et al., 2022a, 2022b), such research may help policymakers plan actionable climate change adaptation and mitigation strategies to address the adverse socioeconomic impacts of CDHWs in the NC region under a warmer climate, such as diminished harvests, water scarcity, mortality, and morbidity.

CRediT authorship contribution statement

Jing Wang: Methodology, Software, Writing – original draft, Visualization, Investigation. **Mingcai Li:** Validation, Data curation, Project administration, Funding acquisition, Writing – review & editing, Investigation. **Yanju Liu:** Validation, Data curation, Writing – review & editing, Investigation. **Jinxin Zhang:** Writing – review & editing, Investigation. **Xiao Zheng:** Writing – review & editing, Investigation.

Declaration of Competing Interest

The authors declare that they have no known competing financial interests or personal relationships that could have appeared to influence the work reported in this paper.

Data availability

Data will be made available on request.

Acknowledgments

The authors are grateful for the insightful comments of the anonymous reviewers. This work is funded by the National Key R & D Program of China (Grant No. 2020YFA0608100). ML and YL are sponsored by the Key Innovation Team of China Meteorological Administration “Climate Change Detection and Response” (CMA2022ZD03).

Appendix A. Supplementary data

Supplementary data to this article can be found online at https://doi.org/10.1016/j.atmosres.2023.106727.

References

Alexander, L., 2011. Extreme heat rooted in dry soils. Nat. Geosci. 4 (1), 12–13.

Ali, S.M., Martius, O., Röthlisberger, M., 2021. Recurrent rossby wave packets modulate the persistence of dry and wet spells across the globe. Geophys. Res. Lett. 48 (5) e2020GL091452.

Alizadeh, M.R., Adamowski, J., Nikoo, M.R., AghaKouchak, A., Dennison, P., Sadegh, M., 2020. A century of observations reveals increasing likelihood of continental-scale compound dry-hot extremes. Science. Advances 6 (39) eaaz4571.

CDC, 2004. Extreme Heat: A Prevention Guide to Promote Your Personal Health and Safety. http://www.bt.cdc.gov/disasters/extremeheat/heat_guide.asp.

Chen, H., Zhao, L., Cheng, L., Zhang, Y., Wang, H., Gu, K., Bao, J., Yang, J., Liu, Z., Huang, J., Chen, Y., Gao, X., Xu, Y., Wang, C., Cai, W., Gong, P., Luo, Y., Liang, W., Huang, C., 2022a. Projections of heatwave-attributable mortality under climate change and future population scenarios in China. Lancet Reg. Health - West. Pac. 28, 100582.

Chen, H., Zhao, L., Dong, W., Cheng, L., Cai, W., Yang, J., Bao, J., Liang, X.-Z., Hajat, S., Gong, P., Liang, W., Huang, C., 2022b. Spatiotemporal variation of mortality burden attributable to heatwaves in China, 1979–2020. Sci. Bull. 67 (13), 1340–1344.

Ciais, P., Reichstein, M., Viovy, N., Granier, A., Ogée, J., Allard, V., Aubinet, M., Buchmann, N., Bernhofer, C., Carrara, A., Chevallier, F., De Noblet, N., Friend, A.D., Friedlingstein, P., Grünwald, T., Heinesch, B., Keronen, P., Knohl, A., Krinner, G., Loustau, D., Manca, G., Matteucci, G., Miglietta, F., Ourcival, J.M., Papale, D., Pilegaard, K., Rambal, S., Seufert, G., Soussana, J.F., Sanz, M.J., Schulze, E.D., Vesala, T., Valentini, R., 2005. Europe-wide reduction in primary productivity caused by the heat and drought in 2003. Nature 437 (7058), 529–533.

Coffel, E.D., Horton, R.M., de Sherbinin, A., 2018. Temperature and humidity based projections of a rapid rise in global heat stress exposure during the 21st century. Environ. Res. Lett. 13 (1), 014001.

Cook, B.I., Mankin, J.S., Marvel, K., Williams, A.P., Smerdon, J.E., Anchukaitis, K.J., 2020. Twenty-first Century Drought Projections in the CMIP6 Forcing scenarios. Earth's Future 8 (6) e2019EF001461.

Dai, A., 2013. Increasing drought under global warming in observations and models. Nat. Clim. Chang. 3 (1), 52–58.

Ding, T., Yuan, Y., Gao, H., Li, W., 2020. Impact of the North Atlantic Sea surface temperature on the summer high temperature in northern China. Int. J. Climatol. 40 (4), 2296–2309.

Easterling, D.R., Meehl, G.A., Parmesan, C., Changnon, S.A., Karl, T.R., Mearns, L.O., 2000. Climate extremes: Observations, modeling, and impacts. Science 289 (5487), 2068.

Eischeid, J.K., Hoerling, M.P., Quan, X.W., Diaz, H.F., 2022. Diagnosing Hawaii's recent drought. J. Clim. 35 (13), 3997–4012.

Feng, L., Li, T., Yu, W., 2014. Cause of severe droughts in Southwest China during 1951–2010. Clim. Dyn. 43 (7), 2033–2042.

Gao, M., Wang, B., Yang, J., Dong, W., 2018. Are peak summer sultry heat wave days over the Yangtze–Huaihe River basin predictable? J. Clim. 31 (6), 2185–2196.

Geirinhas, J.L., Russo, A., Libonati, R., Sousa, P.M., Miralles, D.G., Trigo, R.M., 2021. Recent increasing frequency of compound summer drought and heatwaves in Southeast Brazil. Environ. Res. Lett. 16 (3), 034036.

Gill, A.E., 1980. Some simple solutions for heat-induced tropical circulation. Q. J. R. Meteorol. Soc. 106 (449), 447–462.

Greve, P., Orlowsky, B., Mueller, B., Sheffield, J., Reichstein, M., Seneviratne, S.I., 2014. Global assessment of trends in wetting and drying over land. Nat. Geosci. 7 (10), 716–721.

Ha, K.-J., Seo, Y.-W., Yeo, J.-H., Timmermann, A., Chung, E.-S., Franzke, C.L.E., Chan, J. C.L., Yeh, S.-W., Ting, M., 2022. Dynamics and characteristics of dry and moist heatwaves over East Asia. NPJ Clim. Atmos. Sci. 5 (1), 49.

Ham, Y.-G., Kang, S.-Y., Jeong, Y., Jeong, J.-H., Li, T., 2022. Large-scale Sea surface temperature forcing contributed to the 2013–17 record-breaking meteorological drought in the Korean Peninsula. J. Clim. 35 (12), 3767–3783.

Hao, Z., Hao, F., Singh, V.P., Ouyang, W., 2017. Quantitative risk assessment of the effects of drought on extreme temperature in eastern China. J. Geophys. Res.-Atmos. 122 (17), 9050–9059.

Hao, Z., Hao, F., Singh, V.P., Zhang, X., 2018a. Changes in the severity of compound drought and hot extremes over global land areas. Environ. Res. Lett. 13 (12), 124022.

Hao, Z., Hao, F., Singh, V.P., Zhang, X., 2018b. Quantifying the relationship between compound dry and hot events and El Niño–southern Oscillation (ENSO) at the global scale. J. Hydrol. 567, 332–338.

Hao, Z., Hao, F., Xia, Y., Feng, S., Sun, C., Zhang, X., Fu, Y., Hao, Y., Zhang, Y., Meng, Y., 2022. Compound droughts and hot extremes: Characteristics, drivers, changes, and impacts. Earth Sci. Rev. 235, 104241.

Hayes, M., Svoboda, M., Wall, N., Widhalm, M., 2011. The Lincoln declaration on drought indices: Universal meteorological drought index recommended. Bull. Am. Meteorol. Soc. 92 (4), 485–488.

He, Y., Fang, J., Xu, W., Shi, P., 2022. Substantial increase of compound droughts and heatwaves in wheat growing seasons worldwide. Int. J. Climatol. 42 (10), 5038–5054.

Hersbach, H., Bell, B., Berrisford, P., Hirahara, S., Horányi, A., Muñoz-Sabater, J., Nicolas, J., Peubey, C., Radu, R., Schepers, D., Simmons, A., Soci, C., Abdalla, S., Abellan, X., Balsamo, G., Bechtold, P., Biavati, G., Bidlot, J., Bonavita, M., De Chiara, G., Dahlgren, P., Dee, D., Diamantakis, M., Dragani, R., Flemming, J., Forbes, R., Fuentes, M., Geer, A., Haimberger, L., Healy, S., Hogan, R.J., Hólm, E., Janisková, M., Keeley, S., Laloyaux, P., Lopez, P., Lupu, C., Radnoti, G., de Rosnay, P., Rozum, I., Vamborg, F., Villaume, S., Thépaut, J.-N., 2020. The ERA5 global reanalysis. Q. J. R. Meteorol. Soc. 146 (730), 1999–2049.

Hettiarachchi, S., Wasko, C., Sharma, A., 2022. Do longer dry spells associated with warmer years compound the stress on global water resources? Earth's. Future 10 (2) e2021EF002392.

Hu, S., Zhou, T., Wu, B., 2021. Impact of developing ENSO on Tibetan Plateau summer rainfall. J. Clim. 34 (9), 3385–3400.

Huang, B.Y., Thorne, P.W., Banzon, V.F., Boyer, T., Chepurin, G., Lawrimore, J.H., Menne, M.J., Smith, T.M., Vose, R.S., Zhang, H.M., 2017. Extended Reconstructed Sea Surface Temperature, version 5 (ERSSTv5): upgrades, validations, and intercomparisons. J. Clim. 30 (20), 8179–8205.

Huangfu, J., Tang, Y., Wang, L., Chen, W., Huang, R., Ma, T., 2022. Joint influence of the quasi-biennial oscillation and Indian Ocean basin mode on tropical cyclone occurrence frequency over the western North Pacific. Clim. Dyn. 59 (11), 3439–3449.

Ionita, M., Caldarescu, D.E., Nagavciuc, V., 2021. Compound hot and dry events in Europe: variability and large-scale drivers. Front. Clim. 3, 688991.

Iyakaremye, V., Zeng, G., Yang, X., Zhang, G., Ullah, I., Gahigi, A., Vuguziga, F., Asfaw, T.G., Ayugi, B., 2021. Increased high-temperature extremes and associated population exposure in Africa by the mid-21st century. Sci. Total Environ. 790, 148162.

Jiang, X., Shu, J., Wang, X., Huang, X., Wu, Q., 2017. The roles of convection over the western Maritime Continent and the Philippine Sea in interannual variability of summer rainfall over Southwest China. J. Hydrometeorol. 18 (7), 2043–2056.

Jiang, J., Su, T., Liu, Y., Wu, G., Yu, W., Li, J., 2022. Southeast China extreme drought event in August 2019: context of coupling of midlatitude and tropical systems. J. Clim. 35 (22), 3699–3713.

Kanamitsu, M., Ebisuzaki, W., Woollen, J., Yang, S.K., Hnilo, J.J., Fiorino, M., Potter, G. L., 2002. NCEP–DOE AMIP-II reanalysis (R-2). Bull. Am. Meteorol. Soc. 83 (11), 1631–1644.

Kiem, A.S., Johnson, F., Westra, S., van Dijk, A., Evans, J.P., O'Donnell, A., Rouillard, A., Barr, C., Tyler, J., Thyer, M., Jakob, D., Woldemeskel, F., Sivakumar, B., Mehrotra, R., 2016. Natural hazards in Australia: droughts. Clim. Chang. 139 (1), 37–54.

Kong, Q., Guerreiro, S.B., Blenkinsop, S., Li, X.-F., Fowler, H.J., 2020. Increases in summertime concurrent drought and heatwave in Eastern China. Weather Clim. Extremes 28, 100242.

Li, H., Chen, H., Wang, H., Sun, J., Ma, J., 2018. Can Barents Sea ice decline in spring enhance summer hot drought events over Northeastern China? J. Clim. 31 (12), 4705–4725.

Li, M., Luo, D., Yao, Y., Zhong, L., 2020. Large-scale atmospheric circulation control of summer extreme hot events over China. Int. J. Climatol. 40 (3), 1456–1476.

Li, X., Xu, Y., Wang, J., Wu, J., Song, C., Li, M., 2021a. A possible remote tropical forcing for the interannual variability of peak summer muggy hot days in Northeast China. Atmos. Res. 264, 105860.

Li, X., Wang, C., Lan, J., 2021b. Role of the South China Sea in Southern China rainfall: meridional moisture flux transport. Clim. Dyn. 56 (7), 2551–2568.

Libonati, R., Geirinhas, J.L., Silva, P.S., Russo, A., Rodrigues, J.A., Belém, L.B.C., Nogueira, J., Roque, F.O., DaCamara, C.C., Nunes, A.M.B., Marengo, J.A., Trigo, R. M., 2022. Assessing the role of compound drought and heatwave events on unprecedented 2020 wildfires in the Pantanal. Environ. Res. Lett. 17 (1), 015005.

Liebmann, B., Smith, C.A., 1996. Description of a complete (interpolated) outgoing longwave radiation dataset. Bull. Am. Meteorol. Soc. 77 (6), 1275–1277.

Lu, X., Hong, J., Zhang, L., Cooper, O.R., Schultz, M.G., Xu, X., Wang, T., Gao, M., Zhao, Y., Zhang, Y., 2018. Severe surface ozone pollution in China: a global perspective. Environ. Sci. Technol. Lett. 5 (8), 487–494.

Lu, X., Zhang, L., Wang, X., Gao, M., Li, K., Zhang, Y., Yue, X., Zhang, Y., 2020. Rapid increases in warm-season surface ozone and resulting health impact in China since 2013. Environ. Sci. Technol. Lett. 7 (4), 240–247.

Luo, M., Ning, G., Xu, F., Wang, S., Liu, Z., Yang, Y., 2020. Observed heatwave changes in arid Northwest China: Physical mechanism and long-term trend. Atmos. Res. 242, 105009.

Ma, F., Yuan, X., Jiao, Y., Ji, P., 2020. Unprecedented Europe heat in June–July 2019: risk in the historical and future context. Geophys. Res. Lett. 47 (11) e2020GL087809.

Mazdiyasni, O., AghaKouchak, A., 2015. Substantial increase in concurrent droughts and heatwaves in the United States. Proc. Natl. Acad. Sci. U. S. A. 112 (37), 11484–11489.

Mckee, T.B., Doesken, N.J., Kleist, J., 1993. The relationship of drought frequency and duration to time scales. In: Paper Presented at 8th Conference on Applied Climatology, Anaheim.

Meque, A., Pinto, I., Maúre, G., Beleza, A., 2022. Understanding the variability of heatwave characteristics in southern Africa. Weather Clim. Extremes 38, 100498.

Miralles, D.G., Gentine, P., Seneviratne, S.I., Teuling, A.J., 2019. Land–atmospheric feedbacks during droughts and heatwaves: state of the science and current challenges. Ann. N. Y. Acad. Sci. 1436 (1), 19–35.

Perkins, S.E., 2015. A review on the scientific understanding of heatwaves—their measurement, driving mechanisms, and changes at the global scale. Atmos. Res. 164-165, 242–267.

Sardeshmukh, P.D., Hoskins, B.J., 1988. The generation of global rotational flow by steady idealized tropical divergence. J. Atmos. Sci. 45 (7), 1228–1251.

Seneviratne, S.I., Corti, T., Davin, E.L., Hirschi, M., Jaeger, E.B., Lehner, I., Orlowsky, B., Teuling, A.J., 2010. Investigating soil moisture–climate interactions in a changing climate: a review. Earth Sci. Rev. 99 (3), 125–161.

Seneviratne, S.I., Donat, M.G., Mueller, B., Alexander, L.V., 2014. No pause in the increase of hot temperature extremes. Nat. Clim. Chang. 4 (3), 161–163.

Serrano-Notivoli, R., Lemus-Canovas, M., Barrao, S., Sarricolea, P., Meseguer-Ruiz, O., Tejedor, E., 2022. Heat and cold waves in mainland Spain: Origins, characteristics, and trends. Weather Clim. Extremes 37, 100471.

Sharma, S., Mujumdar, P., 2017. Increasing frequency and spatial extent of concurrent meteorological droughts and heatwaves in India. Sci. Rep. 7 (1), 15582.

Song, Y., Linderholm, H.W., Chen, D., Walther, A., 2010. Trends of the thermal growing season in China, 1951–2007. Int. J. Climatol. 30 (1), 33–43.

Su, B., Huang, J., Fischer, T., Wang, Y., Kundzewicz, Z.W., Zhai, J., Sun, H., Wang, A., Zeng, X., Wang, G., Tao, H., Gemmer, M., Li, X., Jiang, T., 2018. Drought losses in China might double between the 1.5 °C and 2.0 °C warming. Proc. Natl. Acad. Sci. 115 (42), 10600–10605.

Sun, B., Wang, H., Zhou, B., Li, H., 2019. Interdecadal variation in the synoptic features of mei-yu in the Yangtze River valley region and relationship with the Pacific decadal oscillation. J. Clim. 32 (19), 6251–6270.

Thornthwaite, C.W., 1948. An approach toward a rational classification of climate. Geogr. Rev. 38 (1), 55–94.

Ullah, I., Ma, X., Asfaw, T.G., Yin, J., Iyakaremye, V., Saleem, F., Xing, Y., Azam, K., Syed, S., 2022a. Projected changes in increased drought risks over South Asia under a warmer climate. Earth's Future 10 (10) e2022EF002830.

Ullah, I., Saleem, F., Iyakaremye, V., Yin, J., Ma, X., Syed, S., Hina, S., Asfaw, T.G., Omer, A., 2022b. Projected changes in socioeconomic exposure to heatwaves in South Asia under changing climate. Earth's Future 10 (2) e2021EF002240.

Vautard, R., Boucher, O., van Oldenborgh, G.J., Otto, F., Haustein, K., Vogel, M.M., Seneviratne, S.I., Soubeyroux, J.M., Schneider, M., Drouin, A., Ribes, A., Kreienkamp, F., Stott, P., van Aalst, M., 2019. Human Contribution to the RecordBreaking July 2019 Heat Wave in Western Europe. Retrieved from. https://www.ipsl.fr/en/News/News-releases/Human-contribution-to-the-record-breaking-July-2019-heat-wave-in-Western-Europe.

Vicente-Serrano, S.M., Beguería, S., López-Moreno, J.I., 2010. A multiscalar drought index sensitive to global warming: the standardized precipitation evapotranspiration index. J. Clim. 23 (7), 1696–1718.

Wang, B., Wu, R.G., Fu, X.H., 2000. Pacific–East Asian teleconnection: How does ENSO affect East Asian climate? J. Clim. 13 (9), 1517–1536.

Wang, B., Huang, F., Wu, Z., Yang, J., Fu, X., Kikuchi, K., 2009. Multi-scale climate variability of the South China Sea monsoon: a review. Dyn. Atmos. Oceans 47 (1), 15–37.

Wang, B., Xiang, B., Lee, J.-Y., 2013. Subtropical high predictability establishes a promising way for monsoon and tropical storm predictions. Proc. Natl. Acad. Sci. U. S. A. 110 (8), 2718–2722.

Wang, P., Tang, J., Sun, X., Wang, S., Wu, J., Dong, X., Fang, J., 2017. Heat waves in China: definitions, leading patterns, and connections to large-scale atmospheric circulation and SSTs. J. Geophys. Res.-Atmos. 122 (20), 10,679–10,699.

Wang, P., Yang, Y., Li, H., Chen, L., Dang, R., Xue, D., Li, B., Tang, J., Leung, L.R., Liao, H., 2022a. North China Plain as a hot spot of ozone pollution exacerbated by extreme high temperatures. Atmos. Chem. Phys. 22 (7), 4705–4719.

Wang, Z., Zhang, Q., Sun, S., Wang, P., 2022b. Interdecadal variation of the number of days with drought in China based on the standardized precipitation evapotranspiration index (SPEI). J. Clim. 35 (6), 2003–2018.

Watts, N., Adger, W.N., Agnolucci, P., Blackstock, J., Byass, P., Cai, W., Chaytor, S., Colbourn, T., Collins, M., Cooper, A., Cox, P.M., Depledge, J., Drummond, P., Ekins, P., Galaz, V., Grace, D., Graham, H., Grubb, M., Haines, A., Hamilton, I., Hunter, A., Jiang, X., Li, M., Kelman, I., Liang, L., Lott, M., Lowe, R., Luo, Y., Mace, G., Maslin, M., Nilsson, M., Oreszczyn, T., Pye, S., Quinn, T., Svensdotter, M., Venevsky, S., Warner, K., Xu, B., Yang, J., Yin, Y., Yu, C., Zhang, Q., Gong, P., Montgomery, H., Costello, A., 2015. Health and climate change: policy responses to protect public health. Lancet 386 (10006), 1861–1914.

Wilhite, D.A., 2000. Drought as a natural hazard: Concepts and definitions. In: Wilhite, D.A. (Ed.), Drought: A Global Assessment. Routledge, pp. 3–18.

Wu, J., Gao, X., 2013. A gridded daily observation dataset over China region and comparison with the other datasets (in Chinese). Chin. J. Geophys. 56 (4), 1102–1111.

Wu, X., Hao, Z., Hao, F., Zhang, X., Singh, V.P., Sun, C., 2021. Influence of large-scale circulation patterns on compound dry and hot events in China. J. Geophys. Res.-Atmos. 126 (4) e2020JD033918.

Xie, P., Arkin, P.A., 1997. Global precipitation: a 17-year monthly analysis based on gauge observations, satellite estimates, and numerical model outputs. Bull. Am. Meteorol. Soc. 78 (11), 2539–2558.

Xiong, W., Holman, I.P., You, L., Yang, J., Wu, W., 2014. Impacts of observed growing-season warming trends since 1980 on crop yields in China. Reg. Environ. Chang. 14 (1), 7–16.

Xu, K., Lu, R., Kim, B.-J., Park, J.-K., Mao, J., Byon, J.-Y., Chen, R., Kim, E.-B., 2019. Large-scale circulation anomalies associated with extreme heat in South Korea and southern–Central Japan. J. Clim. 32 (10), 2747–2759.

Yang, K., Cai, W., Huang, G., Hu, K., Ng, B., Wang, G., 2022. Increased variability of the western Pacific subtropical high under greenhouse warming. Proc. Natl. Acad. Sci. U. S. A. 119 (23), e2120335119.

Yao, H., Zhao, L., Shen, X., Xiao, Z., Li, Q., 2022. Relationship between summer compound hot and dry extremes in China and the snow cover pattern in the preceding winter. Front. Earth Sci. 10, 834284.

Yeo, S.-R., Yeh, S.-W., Lee, W.-S., 2019. Two Types of Heat Wave in Korea Associated with Atmospheric Circulation Pattern. J. Geophys. Res.-Atmos. 124 (14), 7498–7511.

Yu, R., Zhai, P., 2020a. Changes in compound drought and hot extreme events in summer over populated eastern China. Weather Clim. Extremes 30, 100295.

Yu, R., Zhai, P., 2020b. More frequent and widespread persistent compound drought and heat event observed in China. Sci. Rep. 10 (1), 14576.

Yu, X., He, X., Zheng, H., Guo, R., Ren, Z., Zhang, D., Lin, J., 2014. Spatial and temporal analysis of drought risk during the crop-growing season over Northeast China. Nat. Hazards 71 (1), 275–289.

Zhang, P., Duan, A., 2021. Dipole mode of the precipitation anomaly over the Tibetan Plateau in mid-autumn associated with tropical Pacific-Indian Ocean Sea surface temperature anomaly: role of convection over the northern Maritime Continent. J. Geophys. Res.-Atmos. 126 (20) e2021JD03467.

Zhang, L., Zhou, T., 2015. Drought over East Asia: a review. J. Clim. 28 (8), 3375–3399.

Zhang, L., Xiao, J., Zhou, Y., Zheng, Y., Li, J., Xiao, H., 2016. Drought events and their effects on vegetation productivity in China. Ecosphere 7 (12), e01591.

Zhang, J., Wei, Y., Fang, Z., 2019. Ozone pollution: a major health hazard worldwide. Front. Immunol. 10, 2518.

Zhang, W., Luo, M., Gao, S., Chen, W., Hari, V., Khouakhi, A., 2021. Compound hydrometeorological extremes: drivers, mechanisms and methods. Front. Earth Sci. 9, 673495.

Zhang, T., Tam, C.-Y., Lau, N.-C., Wang, J., Yang, S., Chen, J., Yu, W., Jiang, X., Gao, P., 2022. Influences of the boreal winter Arctic Oscillation on the peak-summer compound heat waves over the Yangtze–Huaihe River basin: the North Atlantic capacitor effect. Clim. Dyn. 59 (7), 2331–2343.

Zhou, Y.P., Xu, K.-M., Sud, Y.C., Betts, A.K., 2011. Recent trends of the tropical hydrological cycle inferred from Global Precipitation Climatology Project and International Satellite Cloud Climatology Project data. J. Geophys. Res.-Atmos. 116. D09101.

Zscheischler, J., Westra, S., van den Hurk, B.J.J.M., Seneviratne, S.I., Ward, P.J., Pitman, A., AghaKouchak, A., Bresch, D.N., Leonard, M., Wahl, T., Zhang, X., 2018. Future climate risk from compound events. Nat. Clim. Chang. 8 (6), 469–477.